CrossMark

J. Fluid Mech. (2018), *vol.* 846, *pp.* 318–340. © Cambridge University Press 2018
doi:10.1017/jfm.2018.249

Geometrical structure analysis of a zero-pressure-gradient turbulent boundary layer

Weipeng Li[1] **and Lipo Wang**[2,†]

[1]School of Aeronautics and Astronautics, Shanghai Jiao Tong University, Shanghai 200240, PR China

[2]UM–SJTU Joint Institute, Shanghai Jiao Tong University, Shanghai 200240, PR China

(Received 16 July 2017; revised 6 March 2018; accepted 15 March 2018;
first published online 4 May 2018)

The present work focuses on the geometrical features of a zero-pressure-gradient turbulent boundary layer based on vectorline segment analysis. In a turbulent vector field, tracing from any non-singular point, along either the vector or the inverse direction, one will reach a local extremum of the vector magnitude. The vectorline between the two local extrema is defined as the vectorline segment corresponding to the given spatial point. Specifically the vectorline segment can be the streamline segment for the velocity vector case, or the vorticity line segment for the vorticity vector case. Such a quantitatively defined and space-filling vectorline segment structure reflects the natural vectorial topology. Because of inhomogeneity in the wall-normal direction, vectorline segments corresponding to the grid points at specified wall-normal distances are sampled for statistics. For streamline segments, the probability density function (p.d.f.) of the normalized segment length in different flow regions matches a model solution, and for vorticity line segments such a p.d.f. in the log-law region and beyond matches the same model solution, which indicates some universality of different flow regions and different vector field structures. Typically the joint p.d.f. of the characteristic parameters of streamline segments presents clear asymmetry, which is closely related to the skewness of the velocity derivative. Moreover, the orientation statistics of vectorline segments, characterized by the coordinate difference between the segment starting point and ending point, have been provided to quantify the flow anisotropy.

Key words: boundary layer structure, turbulent boundary layers, turbulent flows

1. Introduction

To understand turbulent boundary layer flows has always been among the research focuses of the turbulence community. It is widely accepted that in turbulent boundary layers there exist both organized and disorganized motions. The organized part can be characterized by appropriate geometrical descriptions, for instance coherent structures with multi-scales in both space and time. In the near-wall region of a turbulent boundary layer, the dominant dynamic modes are rolls and low-speed streaks (Kline *et al.* 1967; Kim, Moin & Moser 1987; Robinson 1991). Jimenez & Pinelli (1999) analysed the possible mechanisms of turbulence production in this region. In the

† Email address for correspondence: lipo.wang@sjtu.edu.cn

https://doi.org/10.1017/jfm.2018.249 Published online by Cambridge University Press

log region and outer wake regions, the inclined hairpin vortex structure has been extensively studied (Head & Bandyopadhyay 1981; Zhou *et al.* 1999; Adrian 2007; Kang, Choi & Chun 2008; Wu & Moin 2009). Adrian, Meinhart & Tomkins (2000) further found that the hairpin vortices can also appear as a group, which is termed a hairpin packet. At relatively high Reynolds numbers, Kim (1999) proposed the existence of highly energetic very-large-scale structures, which have been verified in subsequent studies (Abe, Kawamura & Choi 2004; Ganapathisubramani, Clemens & Dolling 2006; Monty *et al.* 2007; Marusic & Hutchins 2008). There are also interesting theoretical investigations of the so-called exact coherent structures (Waleffe 1997; Brandt, Henningson & Ponziani 2002; Skufca, Yorke & Eckhardt 2006; Deguchi & Hall 2014).

Coherent structures play an important role in heat transfer and flow drag control. To elucidate the dynamical behaviour of the coherent structures, several techniques have been proposed, including conditional sampling (Antonia 1981), pattern recognition (Eckelmanns *et al.* 1977), proper orthogonal decomposition (POD) (Karhunen 1946), spatial correlations (Ganapathisubramani *et al.* 2006; Chen *et al.* 2014; Mouri 2017), Lagrangian coherent structures (Haller 2015; Schlueter-Kuck & Dabiri 2017) and the vortex-surface field method (Yang & Pullin 2011; Zhao, Yang & Chen 2016). In spite of these numerous efforts, the coherent structures and multi-scale turbulent motions are still not well understood. In summary, the following fundamental issues in structure and geometry analysis need to be addressed:

(i) How can structures be quantitatively and unbiasedly defined, rather than qualitatively described? For instance, the well-studied hairpin vortices, although they can be nicely visualized, are defined with arbitrariness in choosing the contour values. Meanwhile, because by volume such vortices take up only a small portion of the entire flow field, i.e. they are not space-filling, it is not reasonable to understand the entire flow only from the behaviour of hairpin vortices.

(ii) Statistically, how can structures be sufficiently characterized, but in a relatively simple way? Theoretically, flow structures are infinite-dimensional, which makes it is inapplicable to list exhaustively the geometrical parameters of relevance. It is an important prerequisite to reduce the structure dimensionality, at the same time without oversimplification of the physical meaningfulness.

(iii) How can the structure characterization be applied to flow analysis? To achieve this, it is necessary to extract proper characteristic parameters, such as the spatial scale and the flow structure. Considering the scale, for instance, the Fourier representation in wavelength space can be implemented, which in principle is reasonable only for isotropic turbulence. In more complex flows, such as the turbulent boundary layer case (inhomogeneous in the wall-normal direction), the spectral method will then lead to inherent complications associated with the presence of a wall. Therefore it is fundamentally meaningful to characterize the flow structures in a more general sense.

Without a good understanding of these issues, it is difficult to further develop structure analysis beyond illustration and description. Fortunately, in the past decade, some enlightening progress has been made in this framework. For turbulent scalar variables, Wang & Peters (2006) proposed the dissipation element structure to partition a scalar field into space-filling and non-overlapping units, named dissipation elements. Each element consists of grid points whose scalar gradient trajectories share the same local minimum and maximum of the scalar quantity under consideration. Based on

https://doi.org/10.1017/jfm.2018.249 Published online by Cambridge University Press

such spatial decomposition, the original complex system can be better understood from the statistics of the relatively simple units. In principle, dissipation element analysis functions for different scalar fields (Wang & Peters 2008) and different flowing cases, such as isotropic turbulence and turbulent jet mixing (Gampert *et al.* 2011; Gampert, Schaefer & Peters 2013). For the velocity vector case, Wang (2010) developed streamline segment analysis, by which the turbulent velocity field can be decomposed into non-overlapping streamline segments. As will be explained in the next section, streamline segments can be either positive or negative. A main conclusion is that the skewness of velocity derivatives is naturally the kinematic evolution consequence because of the asymmetry between the positive and negative groups. In principle, the streamline segment idea can be implemented directly to different vector quantities. For more application examples and relevant progress, readers are referred to Wang (2012), Schaefer, Gampert & Peters (2013), Boschung *et al.* (2014) and Wang (2014).

The main focus of the present work is to investigate the turbulent boundary layer structure. Here we choose a canonical configuration of the boundary flow over a flat plate with zero streamwise pressure gradient, which from the viewpoint of fundamental research represents the simplest case in many respects. The turbulent boundary layer structure will then be analysed in a quantitative and unbiased manner using vectorline segment analysis. A similar idea can generally be applied to study more complicated features such as very-large-scale motions at high Reynolds numbers.

2. Direct numerical simulations

Direct numerical simulations (DNS) of turbulent flow over a zero-pressure-gradient flat plate is performed. The three-dimensional unsteady compressible Navier–Stokes equations for a perfect gas cast in a conservative form are solved using a finite difference approach. The viscous terms and convective terms are evaluated by a sixth-order central difference scheme and a sixth-order compact difference scheme in transformed curvilinear coordinates (Lele 1992; Visbal & Gaitonde 2002), respectively. To ensure numerical stability an eighth-order low-pass spatial filtering (with the optimization parameter $\alpha_f = 0.493$) (Lele 1992) is applied at each time step on the conservative variables. An alternate directional implicit symmetric Gauss–Seidel (ADI-SGS) scheme (Nishida & Nonomura 2009) is used for the temporal integration with three local sub-iterations to converge the Newton–Raphson sub-iterative process, which can lead to a second-order temporal accuracy. The computational fluid dynamics (CFD) solver has been extensively validated in previous works, for instance for wall-bounded turbulent flows and free jet flows (Nonomura & Fujii 2011; Li, Nonomura & Fujii 2013*a*,*b*).

No-slip and adiabatic boundary conditions are imposed at the bottom wall, and the zero-pressure-gradient condition is used at the outlet and the upper boundary. A recycling and rescaling technique is utilized at the inlet to generate fully developed turbulence without considering a laminar-to-turbulent transition. Specifically, by decomposing the flow field into a time-averaged part and a fluctuating part, the flow properties downstream are recycled to the inlet as the inflow boundary condition according to an appropriate scaling law (Pirozzoli, Bernardini & Grasso 2008). The mean flow field at the inflow is obtained from a two-dimensional Reynolds-averaged Navier–Stokes (RANS) simulation of a flat plate with Spalart–Allmaras turbulence model (Spalart & Allmaras 1992). A weighted function, which was proposed by Lund, Wu & Squires (1998), is used to combine the inner- and outer-layer fluctuations.

https://doi.org/10.1017/jfm.2018.249 Published online by Cambridge University Press

To avoid numerical 'drift' (as discussed in Sagaut *et al.* (2012)), the mean flow fields at the inlet are kept constant, and only the flow density and velocity fluctuations are recycled and rescaled. A dynamic reflection operation proposed by Morgan *et al.* (2011) is applied to eliminate the downstream spurious spatial correlations and reduce unphysical temporal correlations related to the recycling procedure. To more efficiently reach statistically stationary turbulence, the velocity field is initialized using a similar approach developed by Sandham, Yao & Lawal (2003) and Pirozzoli *et al.* (2008). At the statistically stationary state, data samples in a time span of approximately $90\delta_{in}/U_\infty$ are collected for analysis. As justified in the Appendix, such sampling time span is sufficient for statistical convergence.

In the present simulation, the free-stream Mach number is set as $M = U_\infty/a_\infty = 0.3$ in the incompressible regime (Kawai 2016), where U is the streamwise velocity component, a is the speed of sound, and the subscript ∞ denotes the free-stream properties. The Reynolds number based on U_∞ and inlet velocity boundary layer thickness δ_{in} is $Re_{\delta_{in}} = 1.1 \times 10^4$, corresponding to $Re_\theta = 1300$ (based on the momentum boundary layer thickness). To ensure the Courant–Friedrichs–Lewy (CFL) number less than unity, the time step δt is set as $\delta t = 3 \times 10^{-4}\,\delta_{in}/U_\infty$. Because the change of the boundary layer thickness from inlet to outlet is negligibly small (approximately 1 %), in the following analysis the flow is considered as homogeneous in the streamwise direction. With respect to the viscous units, the viscous time step $\delta t^+ = \delta t\, u_\tau^2/\nu$ is less than 0.004, where u_τ denotes the wall friction velocity and ν is the kinematic viscosity. The size of the computational domain is $L_x \times L_y \times L_z = 11\delta_{in} \times 1.7\delta_{in} \times 3\delta_{in}$, where x, y and z stand for the streamwise, wall-normal and spanwise directions, respectively. In total there are $N_x \times N_y \times N_z = 764 \times 179 \times 251$ grid points, which are uniformly distributed in the streamwise direction with $\delta x^+ = 6$ and spanwise direction with $\delta z^+ = 5$, while smoothly stretched in the wall-normal direction from $\delta y^+ = 0.85$ at the wall to $\delta y^+ = 5$ at the boundary layer edge, where $y^+ \approx 410$. As discussed in the Appendix, such resolution is fine enough for the following statistical analyses. In addition, to avoid fluctuations and any reflections from the outlet and the upper boundary, a buffer (sponge) domain is designed, which extends $12\delta_{in}$ with 50 grid points and $25\delta_{in}$ with 40 grid points in the streamwise and wall-normal directions, respectively.

Figure 1 shows an instantaneous snapshot of an isosurface of the second invariant of the complete velocity gradient tensor, coloured with the magnitude of the streamwise velocity. The hairpin structure conforms to the existing literature results. The structure scale evolves to be larger along the wall-normal direction.

To validate the simulation results, figure 2 shows the time-averaged streamwise velocity profile in a semi-logarithmic plot. It can be seen that the present DNS result agrees well with the standard theoretical prediction both in the viscous sublayer as $U^+ = y^+$ and in the log-layer region $U^+ = 2.4\log(y^+) + 5.2$. Figure 3 shows the distribution of Reynolds stress components in both inner scaling and outer scaling, which are in good agreement with the incompressible DNS results at $Re_\theta = 1410$ (Spalart 1988), supersonic DNS data at $M = 1.4$ and $Re_\theta = 1215$ (Pirozzoli, Bernardini & Grasso 2010), and compressible subsonic DNS data at $M = 0.3$ and $Re_\theta = 1010$ (Kawai 2016).

Following the incompressibility condition, a generic form of the turbulent kinetic energy transport equation is formulated as

$$\frac{\mathrm{D}k}{\mathrm{D}t} = P + T + D + \epsilon, \tag{2.1}$$

https://doi.org/10.1017/jfm.2018.249 Published online by Cambridge University Press

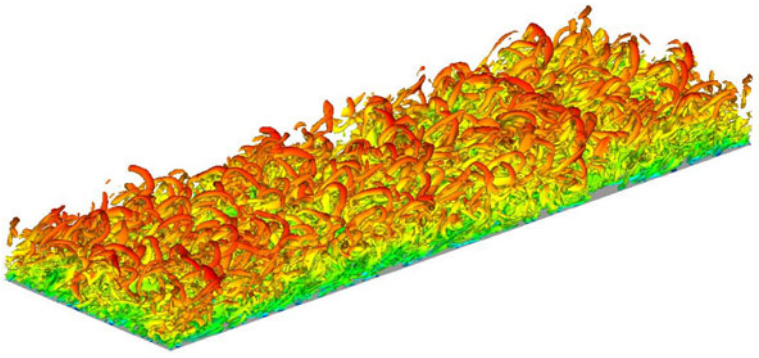


FIGURE 1. (Colour online) Instantaneous snapshot of an isosurface of the second invariant of the complete velocity gradient ($Q = 0.5$), coloured by the streamwise velocity ($0 \leqslant u \leqslant 0.32$).

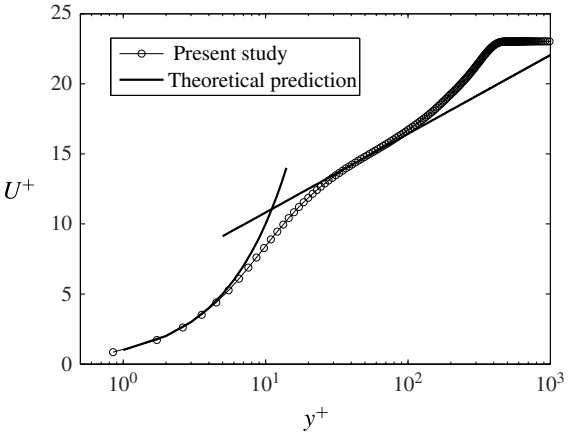


FIGURE 2. Profile of the time-averaged streamwise velocity in wall units.

where the turbulent kinetic energy is defined as $k = \langle u_i' u_i' \rangle / 2$. The production term P, the transport term (by velocity fluctuations and velocity–pressure interaction) T, the viscous diffusion term D and the dissipation term ϵ, respectively, are expressed as

$$P = -\langle u_i' u_j' \rangle \frac{\partial \langle u_j \rangle}{\partial x_i}, \tag{2.2}$$

$$T = -\frac{\partial}{\partial x_i} \left\langle u_i' \left(\frac{p'}{\rho} + \frac{1}{2} u_i' u_i' \right) \right\rangle, \tag{2.3}$$

$$D = \nu \frac{\partial}{\partial x_i} \left\langle u_j' \left(\frac{\partial u_i'}{\partial x_j} + \frac{\partial u_j'}{\partial x_i} \right) \right\rangle, \tag{2.4}$$

$$\epsilon = -\nu \left\langle \left(\frac{\partial u_i'}{\partial x_j} + \frac{\partial u_j'}{\partial x_i} \right) \frac{\partial u_j'}{\partial x_i} \right\rangle. \tag{2.5}$$

Figure 4 shows the turbulent kinetic energy budget in different wall distance scales. Here all the terms are normalized by u_τ^4 / ν. Basically the production and the

https://doi.org/10.1017/jfm.2018.249 Published online by Cambridge University Press

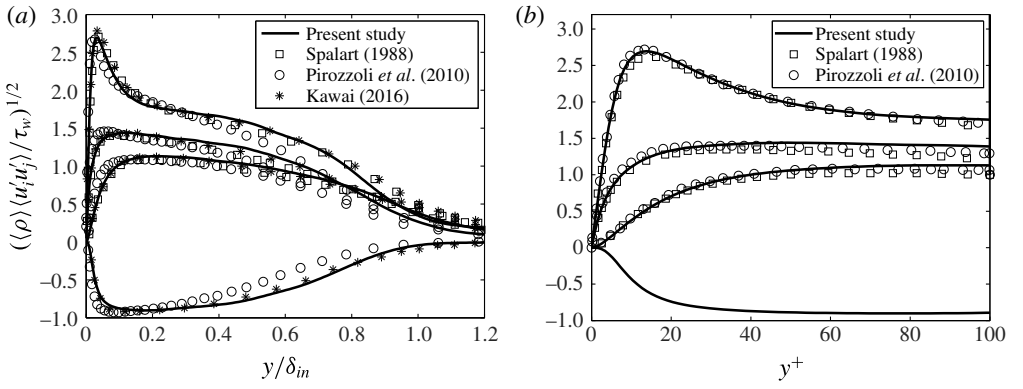


FIGURE 3. Comparison of the calculated Reynolds stress components from the present DNS data (solid line) and the literature results (□, Spalart (1988); ○, Pirozzoli *et al.* (2010); ∗, Kawai (2016)) in (*a*) inner scaling and (*b*) outer scaling for: (top) the streamwise component ($i = j = 1$); (upper middle) the spanwise component ($i = j = 3$); (lower middle) the wall-normal component ($i = j = 2$); and (bottom) the Reynolds shear stress ($i = 1,\ j = 2$).

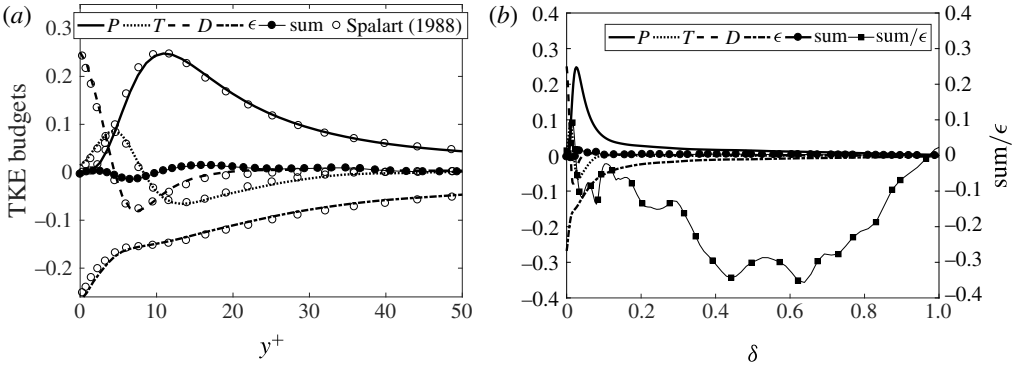


FIGURE 4. Turbulent kinetic energy budget relation (normalized by u_τ^4/ν): (*a*) for the range $0 \leqslant y^+ \leqslant 50$; (*b*) for the entire boundary layer region with the sum error.

dissipation terms are the dominant parts, except in the vicinity of the wall, where turbulent transport and viscous diffusion become important. It can be seen that the sum of budget terms does not entirely vanish. In the near-wall region, the relative sum error sum/ϵ (compared with the dissipation term) is small. Far away from the wall, ϵ is smaller and the absolute value of the relative error is larger, which may be attributed to the relatively short statistical averaging time in the far-wall region. However, tests in the Appendix justify that the statistical averaging time is sufficiently long for satisfactory statistical convergence of quantities relevant for the analysis in the following sections.

3. Vectorline segment analysis

Vectorline segment analysis is implemented to investigate the intrinsic topology of the turbulent boundary layer. In a turbulent vector field $\boldsymbol{v}$ with magnitude $v = |\boldsymbol{v}|$,

https://doi.org/10.1017/jfm.2018.249 Published online by Cambridge University Press

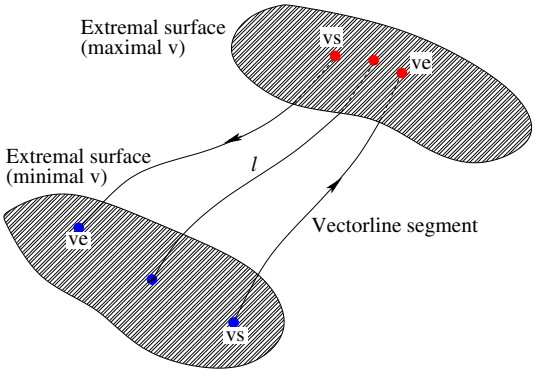


FIGURE 5. (Colour online) Schematic of the vectorline segment structure. From any non-singular point following the vectorline, along either the vector direction or its inverse, one will reach a local extremum of the vector magnitude v. The part of the vectorline between the two local extrema is defined as the vectorline segment corresponding to this spatial point. A segment can be either positive or negative if v increases or decrease along $\boldsymbol{v}$.

except for the singular points, which are defined as the points with zero v, the vector direction is uniquely determined. The vectorline, locally tangent to the vector under consideration, is named 'streamline' for the velocity vector case and 'vorticity line' for the vorticity vector case, respectively. Figure 5 illustrates the schematic of the vectorline segment structure. As introduced by Wang (2010), starting from any non-singular point, along either the vector direction or the inverse direction, one will reach a local extremum of v. The part of the vectorline between the two local extrema of v is defined as a vectorline segment, belonging to the given spatial point. Therefore, within a vectorline segment v changes monotonically from v_s at one end to v_e at the other end along the vector direction. The arclength l of the segment and $\Delta v = v_e - v_s$ are chosen as the characteristic parameters to describe the vectorline segment structure. According to the sign of Δv, a vectorline segment can be either positive (if Δv is positive) or negative (if Δv is negative). In principle, the geometrical statistics of vectorline segments inherit important physics of the turbulent field. It is worth mentioning that, although the vectorline segments are undermined at singular points, whose volume portion is, however, negligibly small, the statistical results will not be influenced.

4. Results and discussion

Velocity and vorticity, two vectors of primary importance in fluid dynamics, will be analysed. The characteristic parameters, which are the arclength and vector magnitude difference, are denoted as l_u and Δu for streamline segments and l_ω and $\Delta\omega$ for vorticity line segments. Note that the segments are defined based on the complete quantities, i.e. the complete velocity and complete vorticity, instead of the fluctuating ones. Figure 6 plots both the vorticity lines and vortex tubes from a field snapshot. Very probably the orientations of both entities are aligned, indicating some geometrical features in common. Meanwhile, when moving away from the wall, on average the vorticity strength decreases and correspondingly the vortex tubes become larger.

https://doi.org/10.1017/jfm.2018.249 Published online by Cambridge University Press

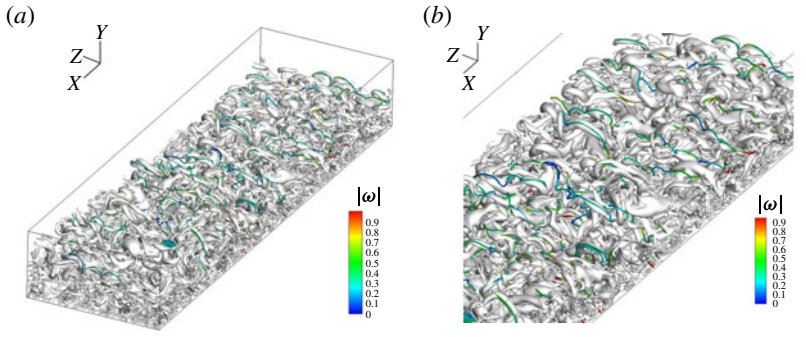


FIGURE 6. (Colour online) The spatial structure of vorticity lines and the vortex tubes (obtained from isosurfaces of the second invariant Q of the velocity gradient): (*a*) an overall view, and (*b*) a local view. On average the magnitude of vorticity increases as the wall distance decreases.

Numerically, to remove the unphysical influence from the domain boundaries, a sub-zone is selected for analysis to ensure the flow (quasi-)homogeneity in the streamwise and spanwise directions. Specifically, the sub-zone size along x, y and z are $7\delta_{in}$, $1.4\delta_{in}$ and δ_{in}, respectively, i.e. from the entire domain $2\delta_{in}$ upstream cut, $2\delta_{in}$ downstream cut, and $0.5\delta_{in}$ cut on both span sides. All the grid points in the sub-zone are used to trace the corresponding vectorline segments. In the present analysis, because of inhomogeneity in the wall-normal direction, vectorline segments corresponding to the grid points at specified wall-normal distances are sampled for statistics.

4.1. *Segment length statistics*

4.1.1. *The mean segment length*

The mean length of vectorline segments quantifies the scale of the local structure. Figure 7 shows for both vectors the dependence of the segment mean length on the wall-normal distance y^+, where the superscript $+$ denotes normalization by the viscous unit. Meanwhile, the Taylor scale, which for boundary layer turbulence is defined as $\lambda(y^+) = \sqrt{10\nu k(y^+)/\epsilon(y^+)}$, is also plotted for comparison. Here $k(y^+)$ and $\epsilon(y^+)$ are the averaged turbulent kinetic energy and the averaged energy dissipation conditioned at specified y^+, respectively. For streamline segments, the mean length $\langle l_u\rangle^+$ decreases quickly in the viscous sublayer ($y^+ < 10$) and buffer layer ($10 < y^+ < 30$), and reaches its minimum in the log-law region at approximately $y^+ \approx 80$. Afterwards $\langle l_u\rangle^+$ increases more and more rapidly until the edge of the boundary layer. For vorticity line segments in the viscous sublayer and part of the buffer layer, the mean length $\langle l_\omega\rangle^+$ decreases slowly and then starts to increase in the entire log-law region and beyond.

Physically, the mean length is dominated by the scale of the local flow structure and the perturbation strength, which can roughly be understood as the local turbulence intensity. On the one hand, the flow structure, for instance shown in figure 1, evolves to be larger from the wall boundary towards the outside, making the segments longer. On the other hand, stronger perturbation, as well as larger turbulence intensity, tends to disturb the flow field to generate more extremal points, making the segments shorter. Within the viscous sublayer, the turbulent intensity increases and then continues to decrease from the buffer region. Therefore the mean length of both the streamline

https://doi.org/10.1017/jfm.2018.249 Published online by Cambridge University Press

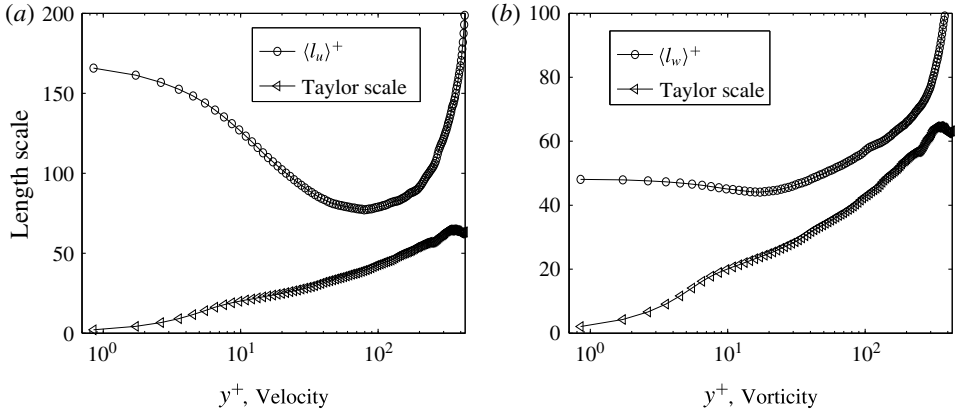


FIGURE 7. The variation of (*a*) $\langle l_u \rangle$ for the streamline segments and (*b*) $\langle l_\omega \rangle$ for the vorticity line segments, as a function of y^+.

segments and vorticity line segments decreases first and then increases. Overall, for vorticity line segments, the mean length $\langle l_\omega \rangle^+$ is much smaller than $\langle l_u \rangle^+$. A sharp difference is that from the solid wall surface $\langle l_u \rangle^+$ decreases largely till $y^+ \approx 80$, while $\langle l_\omega \rangle^+$ decreases weakly in a much shorter range till $y^+ = 20$, which may be an indication that the vorticity line segments are more influenced by the flow structure than turbulence perturbation.

4.1.2. *Probability density function of the length distribution*

More detailed information on the segment length can be viewed from its probability density function (p.d.f.). Work has been done in studying the scale of dissipation elements (Wang & Peters 2006, 2008). Physically, the segment length l is determined by the generation and annihilation of extremal points. On the one hand, turbulent random motion disturbs the flow to generate new extremal points. On the other hand, viscous diffusion annihilates the closely located extremal points to smoothen the flow field. Besides these two abrupt effects, there is another drift velocity representing the continuous change of l. In a general scenario, the evolution of l can be modelled based on a Poisson random cutting–reconnection process. Considering one-dimensional space, each segment is bounded by two extremal points, and all the segments are connected with each other to fill the entire space. Once a newly generated extremal point is added into a segment, it is then cut into two smaller segments. Meanwhile, if two adjacent extremal points merge and then annihilate because of viscous diffusion, two smaller segments can connect to generate a large one. In total, the birth and death of segments are summarized as the following mechanism:

(i) generation by cutting (*GC*);
(ii) generation by reconnection (*GR*);
(iii) removal by cutting (*RC*);
(iv) removal by reconnection (*RR*).

Collecting all the above contributions, together with the drift velocity, one obtains the following equation for the p.d.f. of the segment length l as (Wang & Peters 2006, 2008):

https://doi.org/10.1017/jfm.2018.249 Published online by Cambridge University Press

$$\frac{\partial P(l,t)}{\partial t}+\frac{\partial (v(l)P(l,t))}{\partial l} = \int_0^\infty 2\lambda P(l+z)\,\mathrm{d}z-\lambda l P(l,t) \times \int_0^l 2\mu\frac{z}{l}P(l-z)P(z)\,\mathrm{d}z-2\mu P(l,t). \tag{4.1}$$

Here $v(l)$ is the drift velocity at scale l, λ is the cutting frequency per unit length, and μ is the disappearance rate of extreme points, which can be determined as $\mu = 4D(\partial P(x,t)/\partial x)|_{x=0}$, where D is the fluid viscosity. The four terms on the right-hand side represent *GC*, *RC*, *GR* and *RR*, respectively. In the non-dimensional form, the p.d.f. of $\tilde{l}=l/\langle l\rangle$, i.e. the length scale normalized by its mean $\langle l\rangle$, becomes

$$\frac{\partial P(\tilde{l},t)}{\partial t}+\frac{\partial}{\partial\tilde{l}}(\tilde{v}(\tilde{l})P(\tilde{l},t)) = \Lambda\left[\int_0^\infty 2P(\tilde{l}+\tilde{z},t)\,\mathrm{d}\tilde{z}-\tilde{l}P(\tilde{l},t)\right] +8\frac{\partial P(\tilde{l},t)}{\partial\tilde{l}}\bigg|_{\tilde{l}=0}\left[\int_0^{\tilde{l}}\frac{\tilde{z}}{\tilde{l}}P(\tilde{l}-\tilde{z},t)P(\tilde{z},t)\,\mathrm{d}\tilde{z}-P(\tilde{l},t)\right]. \tag{4.2}$$

Here Λ is an eigenvalue, which can be determined from the p.d.f.'s normalization condition. At the statistically stationary state, there is a dynamic balance under the action of all these mechanisms and the p.d.f. equation (4.2) has a unique time-independent solution. Results from different problems such as the dissipation element scale in passive scalar turbulence (Wang & Peters 2006), the scale distribution in Lagrangian turbulence (Wang 2014) and reactive turbulence (Wang, Chakraborty & Zhang 2013) justify that such a solution is applicable with good generality.

Figure 8 shows the p.d.f. of streamline segment length $\tilde{l}_u$ at different wall-normal distances, in both linear–linear and log–linear coordinates. Compared with the stationary solution of (4.2), the agreement is satisfactory, which implies that the aforementioned smoothing mechanism, the random perturbation mechanism and the continuous drift are generally valid in describing the streamline segment behaviour. It is noteworthy that in the log–linear plot, the p.d.f.'s exponential tail can be explained by a Poisson-like process at the large scale in deriving (4.2).

For vorticity line segments, the length p.d.f. is shown in figure 9, in both linear–linear and log–linear coordinates. Differently from the $\tilde{l}_u$ case, the p.d.f.$(\tilde{l}_\omega)$ at different y^+ is not universal. At larger y^+ (for instance, when $y^+ > 30$) the numerical result matches the solution of (4.2); however, when closer to the wall, the numerical result deviates more from the equation solution. A tentative explanation of such an outcome is that the strong shear stress near the solid wall may invalidate the smoothing and random perturbation mechanisms in deriving (4.2).

4.2. *Joint p.d.f. between the characteristic parameters*

Besides the segment length p.d.f., the joint p.d.f. between the characteristic parameters is more informative. Figure 10 shows such joint p.d.f.s for streamline segments corresponding to grid points at four different wall-normal distances, i.e. $y^+ = 2.6$, $y^+ = 20$, $y^+ = 80$ and $y^+ = 275$, which according to the mean velocity profile in figure 2 represent the typical samples in the viscous sublayer, buffer layer, log-law region and outer layer, respectively. Here Δu is non-dimensionalized by the speed of sound. Each joint p.d.f. has two branches, one with positive Δu and the other with

https://doi.org/10.1017/jfm.2018.249 Published online by Cambridge University Press

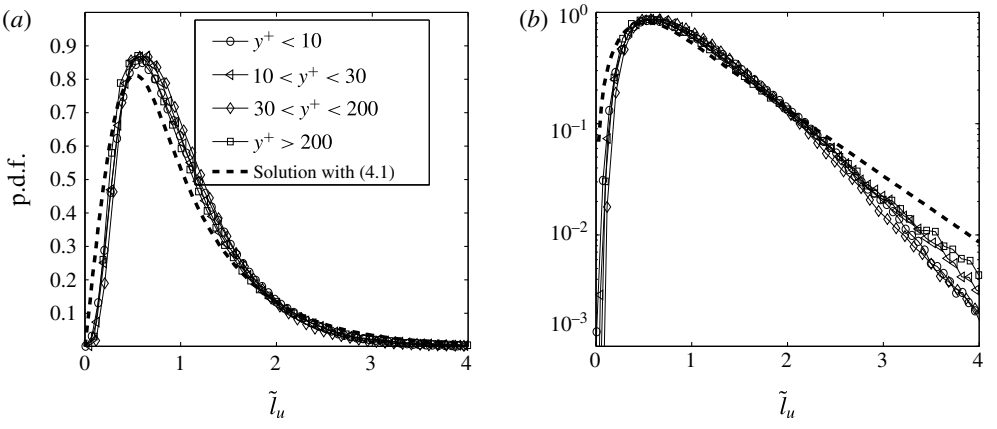


FIGURE 8. P.d.f. of $\tilde{l}_u = l_u/\langle l_u \rangle$ compared with the solution of (4.2) in (*a*) linear–linear coordinates and (*b*) log–linear coordinates.

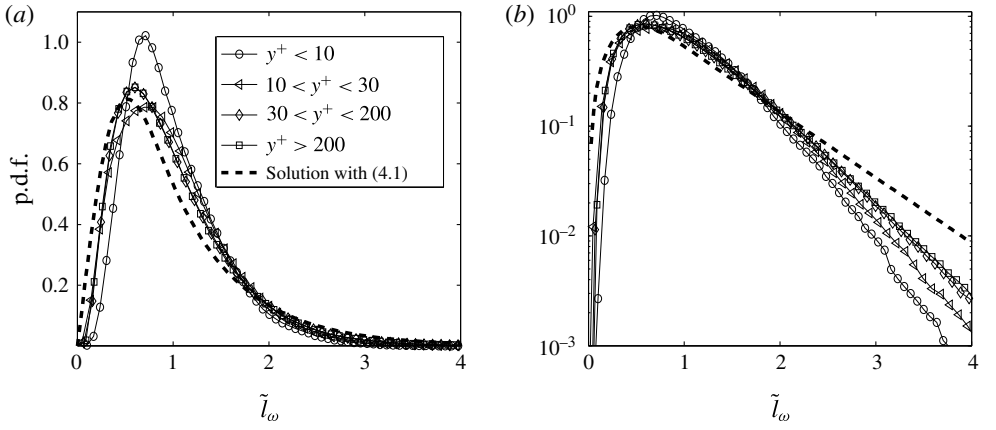


FIGURE 9. P.d.f. of $\tilde{l}_\omega = l_\omega/\langle l_\omega \rangle$ compared with the solution of (4.2) in (*a*) linear–linear coordinates and (*b*) log–linear coordinates.

negative Δu. Interestingly, in the viscous sublayer, these two branches are almost symmetrical. When moving to the buffer layer, the positive branch becomes clearly larger, whereas in the log-law region and outer layer such asymmetry weakens again and finally almost disappears.

Because of the monotonic change of u along the streamline segments, $\Delta u/l_u$ can be interpreted as a kind of averaged velocity derivative. Therefore the asymmetry of the joint p.d.f. implies the unequal contributions from the positive and negative velocity derivative parts in the flow field, which can be approximately quantified by the skewness of the velocity derivative. For the present boundary layer flow, streamline segments are most probably aligned along the streamwise direction. Therefore it is meaningful to investigate the skewness of the streamwise velocity component derivative, i.e.

$$S = \langle (\mathrm{d}u_1/\mathrm{d}x)^3 \rangle / \langle (\mathrm{d}u_1/\mathrm{d}x)^2 \rangle^{3/2}. \tag{4.3}$$

https://doi.org/10.1017/jfm.2018.249 Published online by Cambridge University Press

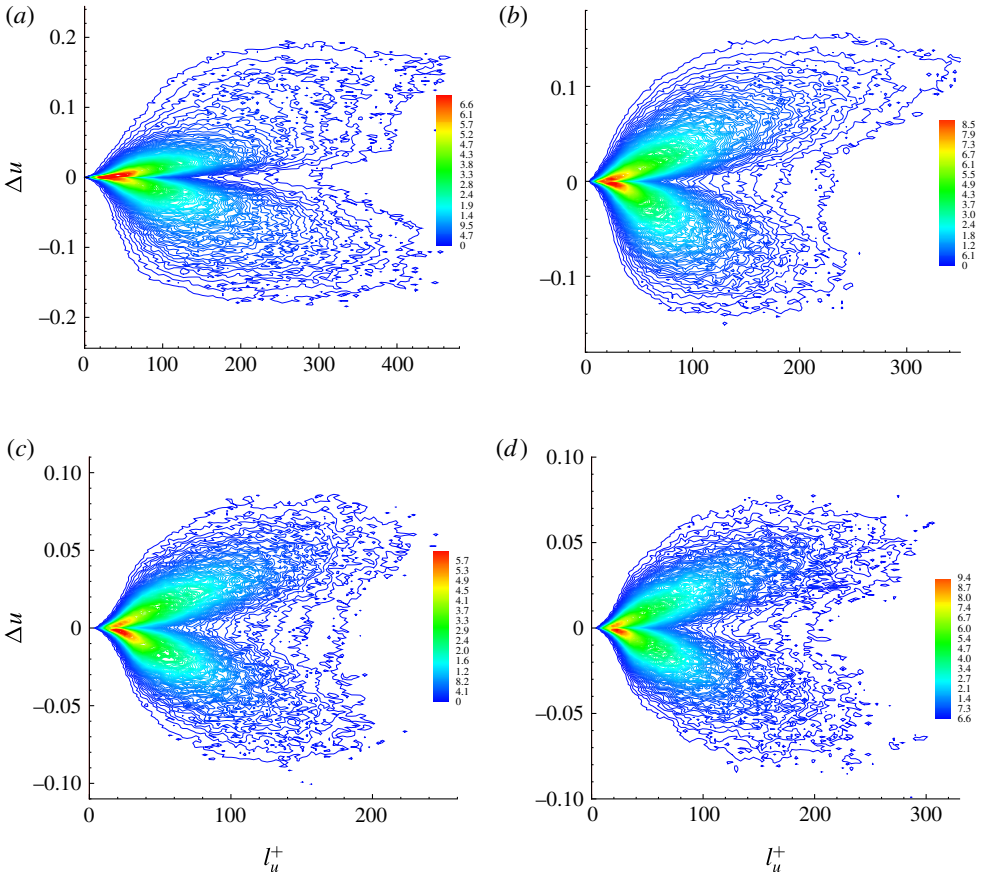


FIGURE 10. (Colour online) Joint p.d.f. of l_u and Δu at different wall-normal distances: (*a*) $y^+ = 2.6$ (in the viscous sublayer); (*b*) $y^+ = 20$ (in the buffer layer); (*c*) $y^+ = 80$ (in the log-law region); and (*d*) $y^+ = 275$ (in the outer layer).

As demonstrated in figure 11, in most of the boundary layer region, the skewness is negative. Around $y^+ = 20$, S reaches its minimum and then increases. A similar behaviour has been observed by Vreman & Kuerten (2014). As y^+ varies, the change of skewness in figure 11 conforms with the change of the joint p.d.f. asymmetry.

Physically, the negative skewness of the velocity derivative represents the average rate of vorticity production through vortex stretching (Taylor 1938; Monin & Yaglom 2007). Vreman & Kuerten (2014) believed that the negative peak is caused by local coherent structures. In the context of streamline segment analysis, the negative skewness can be interpreted from the joint p.d.f. of l_u and Δu. As has been extensively studied (Wang 2010; Boschung *et al.* 2014), the asymmetry of the joint p.d.f. is one of the most important results from streamline segment statistics in isotropic turbulence. Considering an individual streamline segment, the velocity magnitude u along the vector direction will increase monotonically if the segment is positive, or decrease if the segment is negative. Therefore, when evolving with time, positive segments with increasing u tend to be elongated, while negative segments tend to be compressed because of decreasing u along the vector direction. Consequently, on average, the cube

https://doi.org/10.1017/jfm.2018.249 Published online by Cambridge University Press

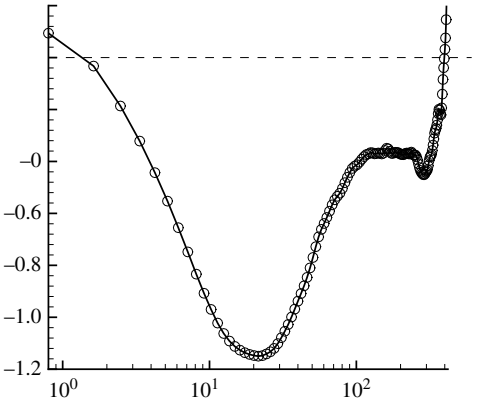


FIGURE 11. Dependence of the skewness of the streamwise velocity component derivative on the wall-normal distance. In coincidence with the asymmetry of the joint p.d.f.s in figure 10, the skewness reaches a minimum in the buffer layer.

of the negative derivative becomes larger, while the cube of the positive derivative becomes smaller, resulting in negative S.

From the joint p.d.f., the conditional mean Δu can be defined as $\langle \Delta u \rangle = \int \Delta u P(\Delta u,\ l_u)\,\mathrm{d}\Delta u$. To differentiate the positive and negative branches, $\langle |\Delta u| \rangle = \int |\Delta u| P(\Delta u,\ l_u)\,\mathrm{d}\Delta u$ are calculated separately for positive segments and negative segments. The results are shown in figure 12. In the log-law region and the outer layer, $\langle |\Delta u| \rangle$ from the positive and negative segments are almost identical for $l_u > 20$, with a scaling exponent approximately 0.8. Differently, in the viscous and buffer sublayers, the positive and negative segments have different conditional mean $\langle |\Delta u| \rangle$ and there is no clear scaling behaviour. Especially in the smaller l_u range, $\langle |\Delta u| \rangle$ from the positive segments is smaller, while in the larger l_u range, $\langle |\Delta u| \rangle$ from the negative segments is smaller.

For vorticity line segments, the joint p.d.f.s between l_ω and $\Delta\omega$ at different y^+ are shown in figure 13. Here $\Delta\omega$ is non-dimensionalized by the speed of sound and the boundary layer thickness. Compared with figure 10, a clear difference is that the positive $\Delta\omega$ and negative $\Delta\omega$ branches are symmetric throughout the boundary layer. The reason is that, for vorticity line segments, the aforementioned kinematic mechanism, leading on average to longer positive streamline segments and shorter negative streamline segments, does not exist (Wang 2012). The positive $\Delta\omega$ and negative $\Delta\omega$ branches are well separated in the viscous sublayer, and then become closer when y^+ increases. Moreover, at larger y^+, $\Delta\omega$ decreases because of smaller velocity gradient and thus vorticity.

Figure 14 plots the conditional mean of $|\Delta\omega|$ as a function of l_ω, which is almost identical for the positive and negative segments. In different boundary layer regions, no obvious scaling can be observed. Especially in the viscous sublayer and buffer layer, $\langle |\Delta\omega| \rangle$ levels off and then drops down at larger l_ω.

4.3. *The segment spatial structure*

We denote the Cartesian coordinate differences between the segment starting point s and ending point e as $\Delta x = x_e - x_s$, $\Delta y = y_e - y_s$ and $\Delta z = z_e - z_s$. In isotropic turbulence without any preference of spatial orientation of the segments, Δx, Δy and

https://doi.org/10.1017/jfm.2018.249 Published online by Cambridge University Press

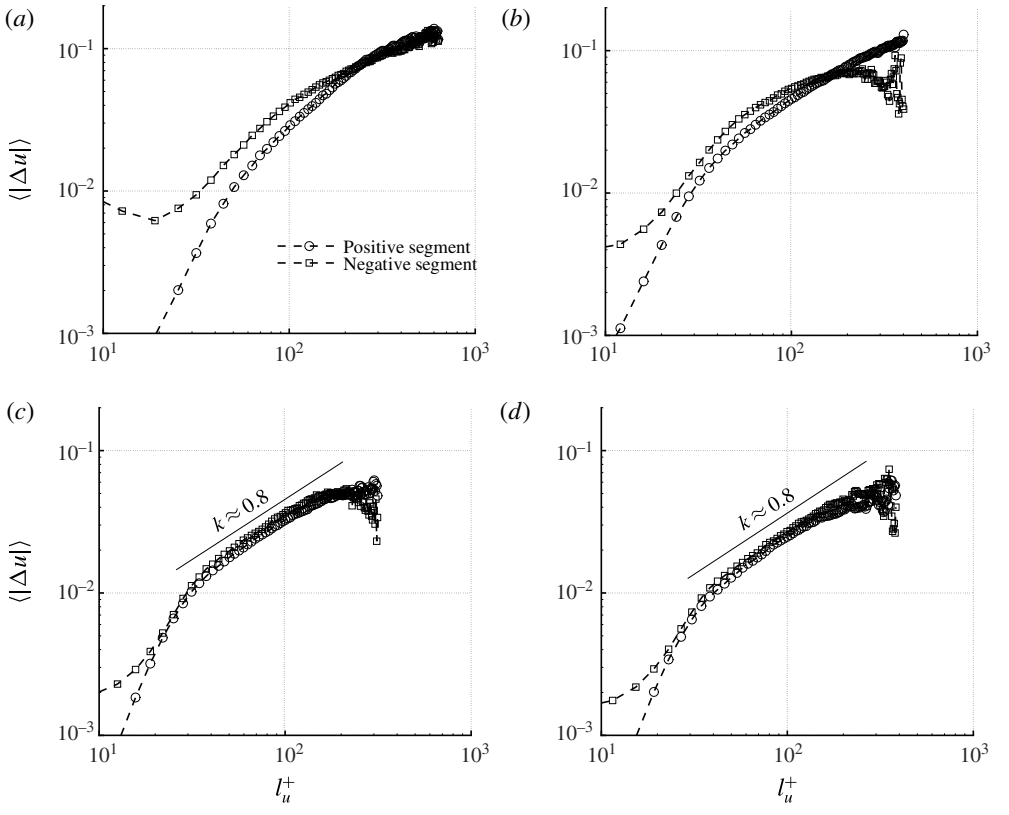


FIGURE 12. The conditional mean of $|\Delta u|$, calculated separately for the positive and negative segments, at different wall-normal distances corresponding to figure 10: (*a*) $y^+ = 2.6$ (in the viscous sublayer); (*b*) $y^+ = 20$ (in the buffer layer); (*c*) $y^+ = 80$ (in the log-law region); and (*d*) $y^+ = 275$ (in the outer layer).

Δz need to be uncorrelated. Therefore, the anisotropy of the turbulent boundary layer can be characterized via the segment orientation statistics.

For streamline segments, the correlations between Δx, Δy and Δz, or between Δx^+, Δy^+ and Δz^+ in the normalized form, are shown in figure 15. The main findings are summarized as follows.

(i) Because of the dominant velocity component along the streamwise direction, segments tend to align with x. Therefore Δx^+ is very probably positive and the magnitude of Δx^+ is much larger than that of Δy^+ and Δz^+, as shown in the joint p.d.f.s between Δx^+ and Δy^+, and between Δx^+ and Δz^+. As y^+ increases, on average Δx^+ first decreases and then increases, which can be explained from the variation of the mean segment length, as shown in figure 7.

(ii) For the joint p.d.f.s between Δx^+ and Δy^+, in the near vicinity of the wall, e.g. $y^+ = 2.6$, because of the boundary confinement, the streamline segments are forced to bend up, and thus Δy^+ is probably positive. When moving to the buffer layer at $y^+ = 20$, the positive Δy^+ part becomes larger. Such an observation indicates that the sweep events in the 'bursting cycle' (Kline *et al.* 1967) predominate the production and regeneration of near-wall turbulence, which is consistent with quadrant analysis (Wallace 2016). From the buffer

https://doi.org/10.1017/jfm.2018.249 Published online by Cambridge University Press

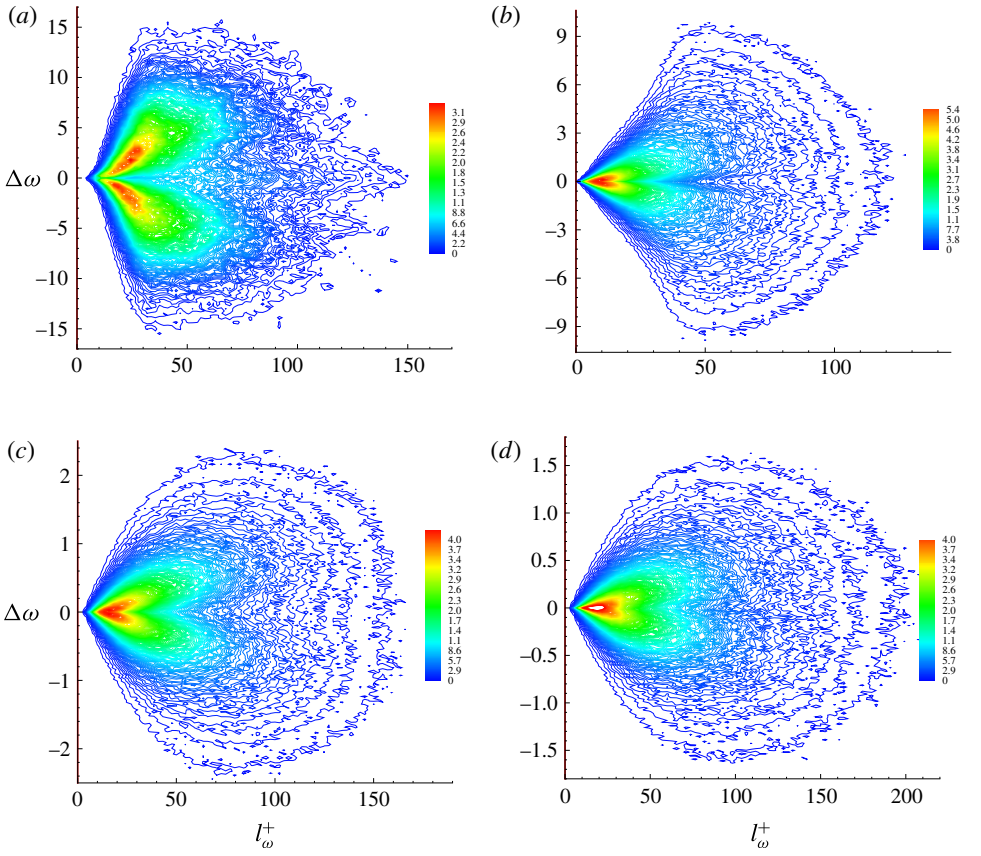


FIGURE 13. (Colour online) Joint p.d.f. of l_ω and $\Delta\omega$ at different wall-normal distances: (*a*) $y^+ = 2.6$ (in the viscous sublayer); (*b*) $y^+ = 20$ (in the buffer layer); (*c*) $y^+ = 80$ (in the log-law region); and (*d*) $y^+ = 275$ (in the outer layer).

layer to the outer layer, the segments then gradually bend down with negative Δy^+. Especially at large y^+ as $y^+ = 275$, the negative Δy^+ part can be clearly observed.

(iii) The joint p.d.f.s between Δy^+ and Δz^+ demonstrate that at $y^+ = 2.6$ on average the magnitude of Δz^+ is much larger than that of Δy^+, which means that the streamline segments are more likely to swing along the spanwise direction than the wall-normal direction. A possible explanation is that the internal shear layers (or vorticity sheets) dominate the dynamic behaviour of the near-wall streaks (Schoppa & Hussain 2002). With the increase of y^+, the magnitude of Δz^+ shrinks gradually and Δy^+ and Δz^+ are comparable. Such a tendency agrees with the change of the turbulence kinetic energy of each velocity component. In principle, Δy^+ and Δz^+ are closely related to the velocity fluctuations along the y and z directions, or equivalently to $\langle u_2'^2 \rangle$ and $\langle u_3'^2 \rangle$, respectively. For y^+ as small as $y^+ = 2.6$, $\langle u_3'^2 \rangle$ is much larger than $\langle u_2'^2 \rangle$, while for larger y^+, $\langle u_3'^2 \rangle$ and $\langle u_2'^2 \rangle$ become closer.

https://doi.org/10.1017/jfm.2018.249 Published online by Cambridge University Press

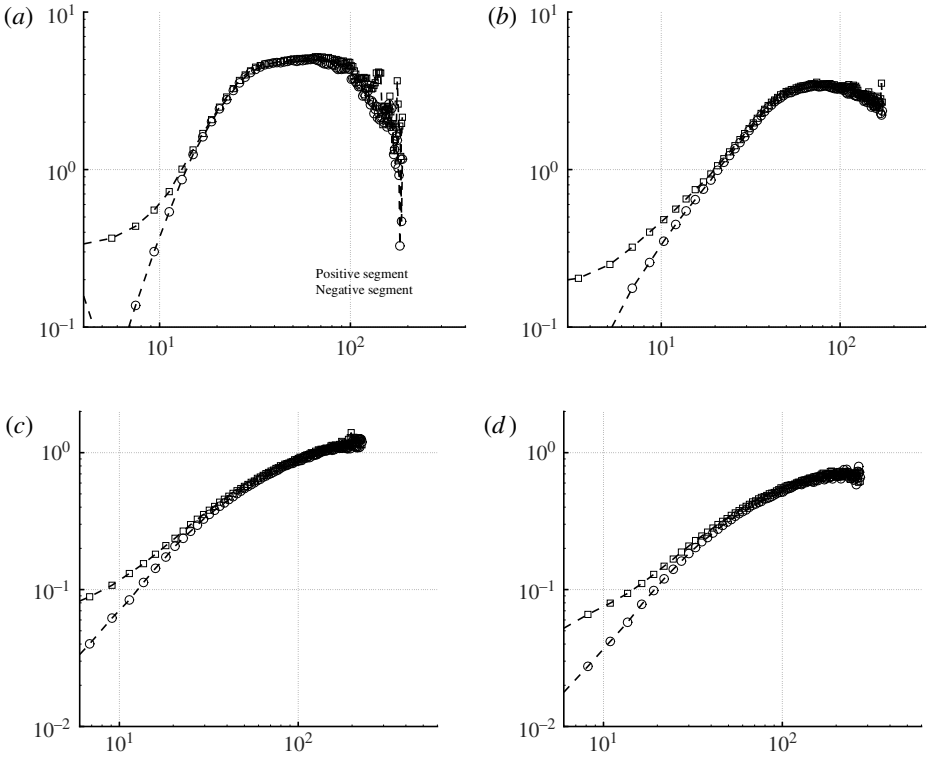


FIGURE 14. The conditional mean of $|\Delta\omega|$, calculated separately for the positive and negative vorticity line segments, at different wall-normal distances corresponding to figure 10: (*a*) $y^+ = 2.6$ (in the viscous sublayer); (*b*) $y^+ = 20$ (in the buffer layer); (*c*) $y^+ = 80$ (in the log-law region); and (*d*) $y^+ = 275$ (in the outer layer).

For vorticity line segments, the main results are presented in figure 16 with the following findings.

(iv) The joint p.d.f.s between Δx^+ and Δy^+ suggest that the magnitudes of Δx^+ and Δy^+ are comparable. At different y^+, the positive Δy^+ part and the negative Δy^+ part are almost symmetric. When y^+ increases, on average the magnitudes of Δy^+ and Δx^+ increase, because of the larger turbulent structure. At $y^+ = 2.6$, Δx^+ and Δy^+ are negatively correlated, while moving away from the wall such correlation becomes positive and Δx^+ on average is marginally larger than Δy^+. The two peaks of the joint p.d.f. may be closely related to the hairpin vortex structure and the orientation of the maximum strain rate (Head & Bandyopadhyay 1981). Further quantitative investigation is needed to better understand the segment statistics.

(v) From the joint p.d.f.s between Δx^+ and Δz^+ and between Δz^+ and Δy^+, we see that at $y^+ = 2.6$, because of the large shear strain rate and thus the vorticity magnitude, the segments are typically oriented in the z direction and Δz^+ is very probably negative. When y^+ increases, the positive Δz^+ part becomes larger because of the stronger perturbation from turbulent eddies, while the negative part remains almost invariant. Overall the negative part is larger. In the log-law region and the outer layer, Δx^+, Δy^+ and Δz^+ are all comparable in magnitude.

https://doi.org/10.1017/jfm.2018.249 Published online by Cambridge University Press

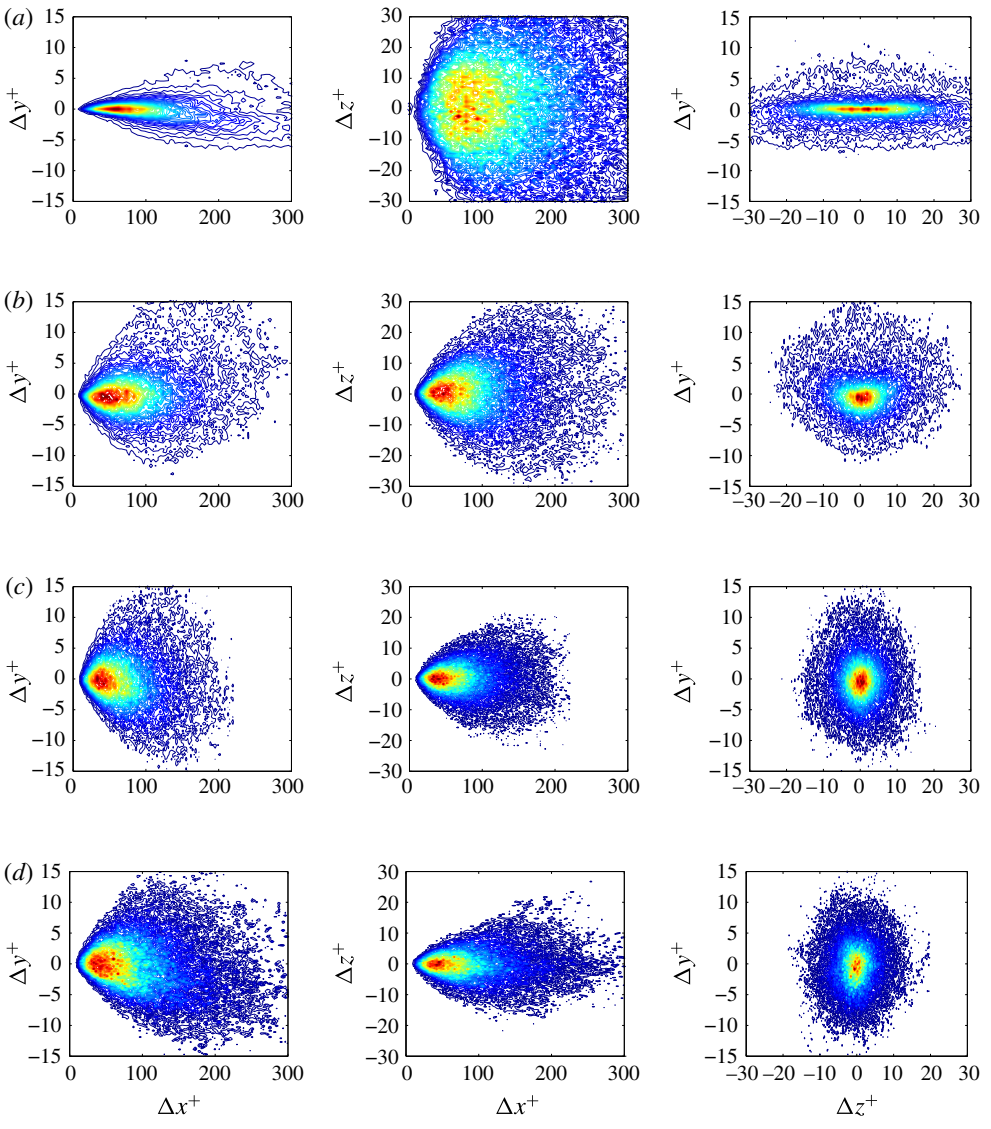


FIGURE 15. (Colour online) For the streamline segments, the joint p.d.f. between the spatial coordinates (Δx, Δy and Δz) at (*a*) $y^+ = 2.6$, (*b*) $y^+ = 20$, (*c*) $y^+ = 80$ and (*d*) $y^+ = 275$.

(vi) The joint p.d.f.s between Δy^+ and Δz^+ are symmetric across the abscissa axis, which means that vorticity line segments have no preference to bend upwards or downwards. When y^+ increases, the positive and negative Δy^+ branches become less separated because the flow is more isotropic.

5. Conclusions

The velocity and vorticity vector fields of a zero-pressure-gradient turbulent boundary layer flow have been investigated based on vectorline segment analysis.

https://doi.org/10.1017/jfm.2018.249 Published online by Cambridge University Press

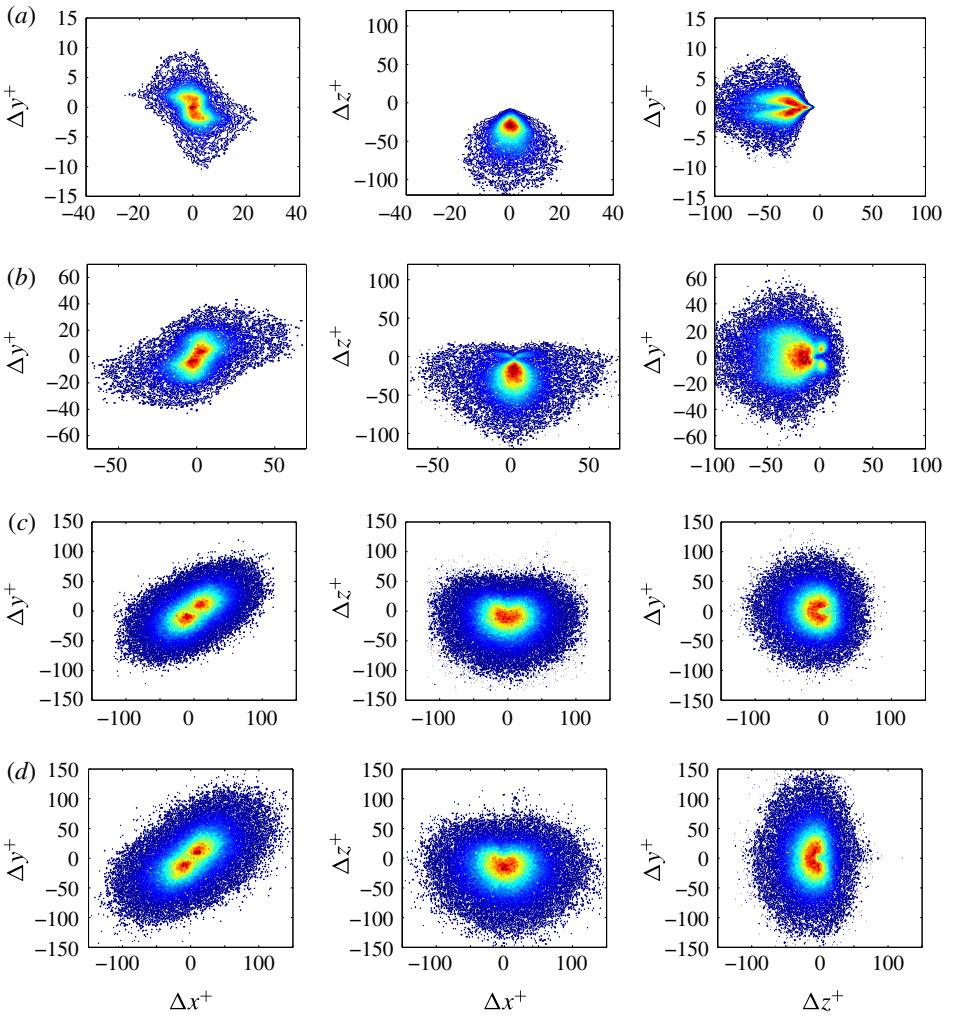


FIGURE 16. (Colour online) For the vorticity line segments, the joint p.d.f. between the spatial coordinates (Δx, Δy and Δz) at (*a*) $y^+ = 2.6$, (*b*) $y^+ = 20$, (*c*) $y^+ = 80$ and (*d*) $y^+ = 275$.

For a specified vector field, the vectorline, a structure independent of the reference frame, inherits important flow characteristics. From any non-singular point, along either the vector or the inverse direction, one will reach a local extremum of the vector magnitude. The part of the vectorline between the two local extremal points is defined as a vectorline segment corresponding to the spatial point under consideration. Each vectorline segment can be characterized with the arclength and the vector magnitude difference. Such a segment structure definition is unbiased (space-filling) and quantitative, which is essentially important for structure analysis and modelling. The main findings based on DNS are summarized as follows.

(1) Different from the isotropic turbulence case, because of flow inhomogeneity, the statistical results need to be conditioned on vectorline segments corresponding to the grid points at specified wall-normal distances. Overall, the mean lengths of

https://doi.org/10.1017/jfm.2018.249 Published online by Cambridge University Press

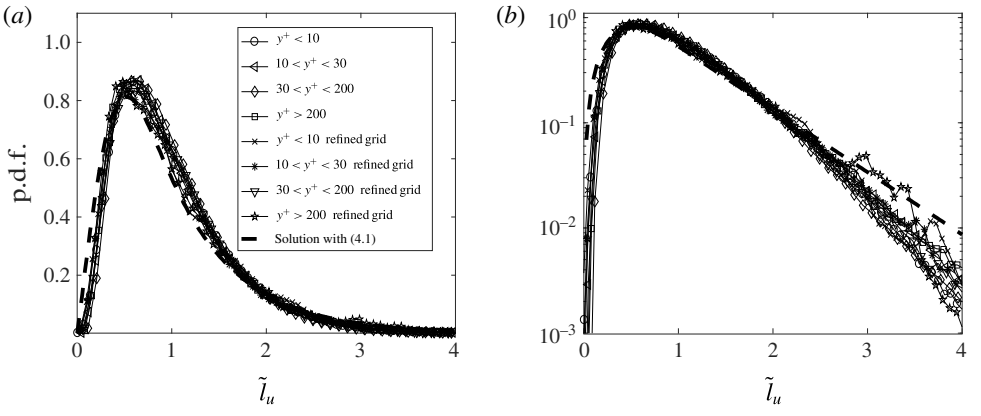


FIGURE 17. Resolution independence check for the p.d.f. of $\tilde{l}_u = l_u/\langle l_u \rangle$.

streamline segments and vorticity line segments have similar dependences on the wall-normal distance. Physically, the mean length is influenced by both the local turbulent eddy size and local turbulent intensity. In the viscous sublayer, the mean length decreases with y^+ because turbulent intensity increases to generate shorter segments. In the log-law region when y^+ increases, the mean length increases because of the larger turbulent eddies and decaying turbulent kinetic energy. Relatively, l_ω decreases more slowly than l_u.

(2) For streamline segments, the probability density function (p.d.f.) of the segment length at different wall-normal distances shows nice universality. The normalized p.d.f.s overlap and can be satisfactorily described by the solution of (4.2), which has been proved to be applicable under various conditions, such as the passive scalar case, reactive turbulence and Lagrangian turbulence. For vorticity line segments, in the near-wall viscous region, the p.d.f.'s universality breaks down. However, in the log-law region and outer layer, the length p.d.f. matches the equation solution.

(3) Kinematically positive streamline segments tend to be stretched and negative streamline segments tend to be compressed, which then leads to asymmetry of the joint p.d.f. between l_u and Δu. Surprisingly, in the viscous sublayer region, such asymmetry almost disappears. From the buffer layer to the log-law region and the outer layer, the asymmetry weakens. The change of skewness of the streamwise velocity derivative along y^+ follows the same tendency. For vorticity line segments, the joint p.d.f. between l_ω and $\Delta\omega$ is symmetric, and the conditional means of $|\Delta\omega|$ for the positive and negative segments are almost identical.

(4) Correlations of the Cartesian coordinate differences (Δx^+, Δy^+ and Δz^+) are also provided to understand the segment orientation statistics and quantify the structure anisotropy. Further investigations are needed to understand the relation between these correlations and the flow topology, such as near-wall low-speed streaks, sweep events and hairpin vortices.

Acknowledgements

The funding support of the National Basic Research Programme of China (973 programme; grant 2014CB744802) and the support of the National Natural Science

https://doi.org/10.1017/jfm.2018.249 Published online by Cambridge University Press

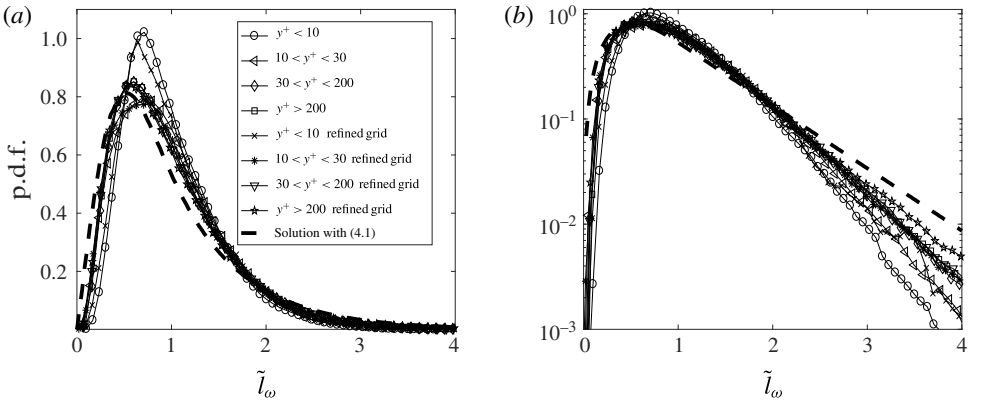


FIGURE 18. Resolution independence check for the p.d.f. of $\tilde{l}_\omega = l_\omega/\langle l_\omega \rangle$.

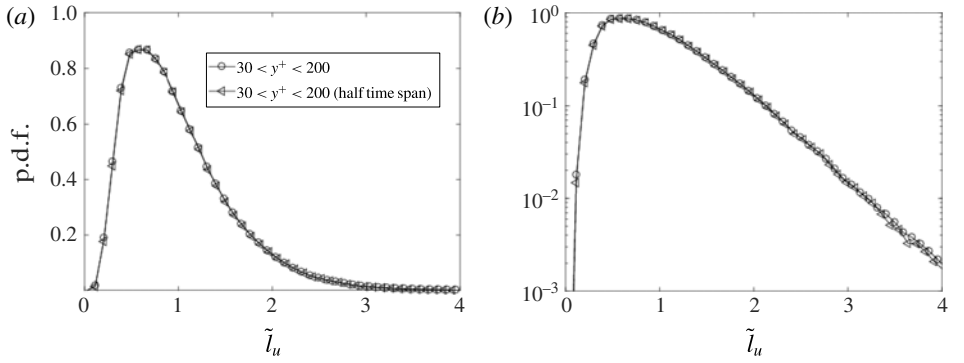


FIGURE 19. Statistical convergence check for the p.d.f. of $\tilde{l}_u$.

Foundation of China (under the grant nos. 11772194 and 91441116) are acknowledged. W.L. also thanks the Centre for High Performance Computing at Shanghai Jiao Tong University for supporting the large-scale computations.

Appendix. Resolution independence and statistical convergence

The current mesh satisfies the DNS resolution requirement, especially along the wall-normal direction. To justify the sufficiency of the resolution, considering that the vector lines and vorticity lines in the near-wall region are basically parallel to the wall, a new mesh set-up is used with doubled grid points along both the streamwise and spanwise directions. The length p.d.f.s of streamline segments are shown in figure 17, and the length p.d.f.s of vorticity line segments are shown in figure 18. It can be seen that the curves from the different mesh set-up cases are quite close. For the high-resolution results, slight scattering at the p.d.f. tails is attributed to the short sampling time span ($30\delta_{in}/U_\infty$) for statistical average.

Meanwhile, to justify the statistical convergence, p.d.f.s of $\tilde{l}_u$ and $\tilde{l}_\omega$ from only half time span samples are also calculated, as shown in figures 19 and 20. Clearly, the differences are negligibly small.

https://doi.org/10.1017/jfm.2018.249 Published online by Cambridge University Press

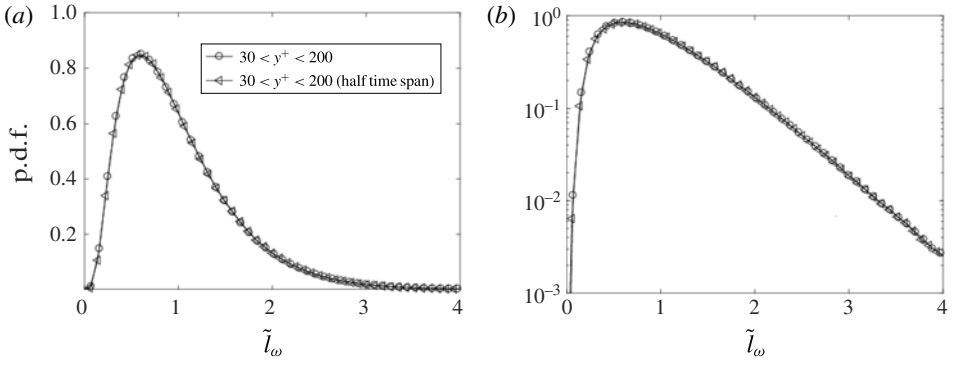


FIGURE 20. Statistical convergence check for the p.d.f. of $\tilde{l}_\omega$.

REFERENCES

ABE, H., KAWAMURA, H. & CHOI, H. 2004 Very large-scale structures and their effects on the wall shear-stress fluctuations in a turbulent channel flow up to $Re_\tau = 640$. *J. Fluids Engng* **126** (5), 835–843.

ADRIAN, R. J., MEINHART, C. D. & TOMKINS, C. D. 2000 Vortex organization in the outer region of the turbulent boundary layer. *J. Fluid Mech.* **422**, 1–53.

ADRIAN, R. J. 2007 Hairpin vortex organization in wall turbulence. *Phys. Fluids* **19**, 041301.

ANTONIA, R. A. 1981 Conditional sampling in turbulence measurement. *Annu. Rev. Fluid Mech.* **13** (1), 131–156.

BOSCHUNG, J., SCHAEFER, P., PETERS, N. & MENEVEAU, C. 2014 The local topology of stream- and vortex lines in turbulent flows. *Phys. Fluids* **26** (4), 045107.

BRANDT, L., HENNINGSON, D. S. & PONZIANI, D. 2002 Weakly nonlinear analysis of boundary layer receptivity to free-stream disturbances. *Phys. Fluids* **14** (4), 1426–1441.

CHEN, J., HUSSAIN, F., PEI, J. & SHE, Z. S. 2014 Velocity–vorticity correlation structure in turbulent channel flow. *J. Fluid Mech.* **742**, 291–307.

DEGUCHI, K. & HALL, P. 2014 Canonical exact coherent structures embedded in high Reynolds number flows. *Proc. R. Soc. Lond.* A **372** (2020), 20130352.

ECKELMANNS, H., NYCHAS, S. G., BRODKEY, R. S. & WALLACE, J. M. 1977 Vorticity and turbulence production in pattern recognized turbulent flow structures. *Phys. Fluids* **20** (20), S225–S231.

GAMPERT, M., GOEBBERT, J. H., SCHAEFER, P., GAUDING, M., PETERS, N., ALDUDAK, F. & OBERLACK, M. 2011 Extensive strain along gradient trajectories in the turbulent kinetic energy field. *New J. Phys.* **13** (4), 043012.

GAMPERT, M., SCHAEFER, P. & PETERS, N. 2013 Experimental investigation of dissipation-element statistics in scalar fields of a jet flow. *J. Fluid Mech.* **724**, 337–366.

GANAPATHISUBRAMANI, B., CLEMENS, N. T. & DOLLING, D. S. 2006 Large-scale motions in a supersonic turbulent boundary layer. *J. Fluid Mech.* **556**, 271–282.

HALLER, G. 2015 Lagrangian coherent structures. *Annu. Rev. Fluid Mech.* **47**, 137–162.

HEAD, M. R. & BANDYOPADHYAY, P. 1981 New aspects of turbulent boundary-layer structure. *J. Fluid Mech.* **107**, 197–337.

JIMENEZ, J. & PINELLI, A. 1999 The autonomous cycle of near-wall turbulence. *J. Fluid Mech.* **389**, 335–359.

KANG, Y. D., CHOI, K. S. & CHUN, H. H. 2008 Direct intervention of hairpin structures for turbulent boundary-layer control. *Phys. Fluids* **20** (10), 101517.

KARHUNEN, K. 1946 Uber lineare Methoden in der Wahrscheinlichkeitsrechnung. *Ann. Acad. Sci. Fenn., Ser. A1, Math. Phys.* **37**, 3–79.

https://doi.org/10.1017/jfm.2018.249 Published online by Cambridge University Press

KAWAI, S. 2016 Direct numerical simulation of transcritical turbulent boundary layers at supercritical pressures with strong real fluid effects. *AIAAA Paper* 2016-1934.

KIM, J., MOIN, P. & MOSER, R. 1987 Turbulence statistics in fully developed channel flow at low Reynolds number. *J. Fluid Mech.* **177**, 133–166.

KIM, K. C. & ADRIAN, R. J. 1999 Very large-scale motion in the outer layer. *Phys. Fluids* **11**, 417–422.

KLINE, S. J., REYNOLDS, W. C., SCHRAUB, F. A. & RUNSTADLER, P. W. 1967 The structure of turbulent boundary layers. *J. Fluid Mech.* **30**, 741–773.

LELE, S. K. 1992 Compact finite difference schemes with spectral-like resolution. *J. Comput. Phys.* **103** (1), 16–42.

LI, W., NONOMURA, T. & FUJII, K. 2013*a* Mechanism of controlling supersonic cavity oscillations using upstream mass injection. *Phys. Fluids* **25** (8), 086101.

LI, W., NONOMURA, T. & FUJII, K. 2013*b* On the feedback mechanism in supersonic cavity flows. *Phys. Fluids* **25** (5), 056101.

LUND, T. S., WU, X. & SQUIRES, K. D. 1998 Generation of turbulent inflow data for spatially-developing boundary layer simulations. *J. Comput. Phys.* **140** (2), 233–258.

MARUSIC, I. & HUTCHINS, N. 2008 Study of the log-layer structure in wall turbulence over a very large range of Reynolds number. *Flow Turbul. Combust.* **81**, 115–130.

MONIN, A. S. & YAGLOM, A. M. 2007 *Statistical Fluid Mechanics*, vol. II. Dover.

MONTY, J. P., STEWART, J. A., WILLIAMS, R. C. & CHONG, M. S. 2007 Large-scale features in turbulent pipe and channel flows. *J. Fluid Mech.* **589**, 147–156.

MORGAN, B., LARSSON, J., KAWAI, S. & LELE, S. K. 2011 Improving low-frequency characteristics of recycling/rescaling inflow turbulence generation. *AIAA J.* **49** (3), 582–597.

MOURI, H. 2017 Two-point correlation in wall turbulence according to the attached-eddy hypothesis. *J. Fluid Mech.* **821**, 343–357.

NISHIDA, H. & NONOMURA, T. 2009 ADI-SGS scheme on ideal magnetohydrodynamics. *J. Comput. Phys.* **228** (9), 3182–3188.

NONOMURA, T. & FUJII, K. 2011 Overexpansion effects on characteristics of Mach waves from a supersonic cold jet. *AIAA J.* **49** (10), 2282–2294.

PIROZZOLI, S., BERNARDINI, M. & GRASSO, F. 2008 Characterization of coherent vortical structures in a supersonic turbulent boundary layer. *J. Fluid Mech.* **613**, 205–231.

PIROZZOLI, S., BERNARDINI, M. & GRASSO, F. 2010 Direct numerical simulation of transonic shock/boundary layer interaction under conditions of incipient separation. *J. Fluid Mech.* **657**, 361–393.

ROBINSON, S. K. 1991 Coherent motions in the turbulent boundary-layer. *Annu. Rev. Fluid Mech.* **23**, 601–639.

SAGAUT, P., GARNIER, E., TROMEUR, E., LARCHEVEQUE, L. & LABOURASSE, E. 2012 Turbulent inflow conditions for large-eddy-simulation of compressible wall-bounded flows. *AIAA J.* **42** (3), 469–477.

SANDHAM, N. D., YAO, Y. F. & LAWAL, A. A. 2003 Large-eddy simulation of transonic turbulent flow over a bump. *Intl J. Heat Fluid Flow* **24** (4), 584–595.

SCHAEFER, P., GAMPERT, M. & PETERS, N. 2013 A model equation for the joint distribution of the length and velocity difference of streamline segments in turbulent flows. *Phys. Fluids* **25** (11), 115107.

SCHLUETER-KUCK, K. L. & DABIRI, J. O. 2017 Coherent structure coloring: identification of coherent structures from sparse data using graph theory. *J. Fluid Mech.* **811**, 468–486.

SCHOPPA, W. & HUSSAIN, F. 2002 Coherent structure generation in near-wall turbulence. *J. Fluid Mech.* **453**, 57–108.

SKUFCA, J. D., YORKE, J. A. & ECKHARDT, B. 2006 Edge of chaos in a parallel shear flow. *Phys. Rev. Lett.* **96**, 174101.

SPALART, P. R. 1988 Direct simulation of a turbulent boundary layer up to $Re_\theta = 1410$. *J. Fluid Mech.* **187**, 61–98.

SPALART, P. R. & ALLMARAS, S. R. 1992 A one equation turbulence model for aerodinamic flows. *AIAA Paper* 1992-0439.

https://doi.org/10.1017/jfm.2018.249 Published online by Cambridge University Press

TAYLOR, G. I. 1938 Production and dissipation of vorticity in a turbulent fluid. *Proc. R. Soc. Lond.* A **164**, 15–23.

VISBAL, M. R. & GAITONDE, D. V. 2002 On the use of higher-order finite-difference schemes on curvilinear and deforming meshes. *J. Comput. Phys.* **181** (1), 155–185.

VREMAN, A. W. & KUERTEN, J. G. M. 2014 Statistics of spatial derivatives of velocity and pressure in turbulent channel flow. *Phys. Fluids* **26**, 085103.

WALEFFE, F. 1997 On a self-sustaining process in shear flows. *Phys. Fluids* **9**, 883–900.

WALLACE, J. M. 2016 Quadrant analysis in turbulence research: history and evolution. *Annu. Rev. Fluid Mech.* **48**, 131–158.

WANG, L. 2010 On properties of fluid turbulence along streamlines. *J. Fluid Mech.* **648**, 183–203.

WANG, L. 2012 Structures of the vorticity tube segment in turbulence. *Phys. Fluids* **24**, 045101.

WANG, L. 2014 Analysis of the Lagrangian path structures in fluid turbulence. *Phys. Fluids* **26**, 045014.

WANG, L., CHAKRABORTY, N. & ZHANG, J. 2013 Streamline segment analysis of turbulent premixed flames. *Proc. Combust. Inst.* **34**, 1401–1409.

WANG, L. & PETERS, N. 2006 The length-scale distribution function of the distance between extremal points in passive scalar turbulence. *J. Fluid Mech.* **554**, 457–475.

WANG, L. & PETERS, N. 2008 Length-scale distribution functions and conditional means for various fields in turbulence. *J. Fluid Mech.* **608**, 113–138.

WU, X. & MOIN, P. 2009 Forest of hairpins in a low-Reynolds-number zero-pressure-gradient flat-plate boundary layer. *Phys. Fluids* **21** (9), 091106.

YANG, Y. & PULLIN, D. 2011 Evolution of vortex-surface fields in viscous Taylor–Green and Kida–Pelz flows. *J. Fluid Mech.* **685**, 146–164.

ZHAO, Y., YANG, Y. & CHEN, S. 2016 Vortex reconnection in the late transition in channel flow. *J. Fluid Mech.* **802**, R4.

ZHOU, J., ADRIAN, R. J., BALACHANDAR, S. & KENDALL, T. M. 1999 Mechanisms for generating coherent packets of hairpin vortices in channel flow. *J. Fluid Mech.* **387**, 353–396.

https://doi.org/10.1017/jfm.2018.249 Published online by Cambridge University Press